CrossMark

GAMMA-RAY BURST REVERSE SHOCK EMISSION IN EARLY RADIO AFTERGLOWS

Lekshmi Resmi[1] and Bing Zhang[2]
[1] Indian Institute of Space Science & Technology, Trivandrum, India; l.resmi@iist.ac.in
[2] Department of Physics and Astronomy, University of Nevada, Las Vegas, USA

ABSTRACT

Reverse shock (RS) emission from gamma-ray bursts is an important tool in investigating the nature of the ejecta from the central engine. If the magnetization of the ejecta is not high enough to suppress the RS, a strong RS emission component, usually peaking in the optical/IR band early on, would provide an important contribution to early afterglow light curve. In the radio band, synchrotron self-absorption may suppress early RS emission and also delay the RS peak time. In this paper, we calculate the self-absorbed RS emission in the radio band under different dynamical conditions. In particular, we stress that the RS radio emission is subject to self-absorption in both RSs and forward shocks (FSs). We calculate the ratio between the RS to FS flux at the RS peak time for different frequencies, which is a measure of the detectability of the RS emission component. We then constrain the range of physical parameters for a detectable RS, in particular the role of magnetization. We notice that unlike optical RS emission which is enhanced by moderate magnetization, moderately magnetized ejecta do not necessarily produce a brighter radio RS due to the self-absorption effect. For typical parameters, the RS emission component would not be detectable below 1 GHz unless the medium density is very low (e.g., $n < 10^{-3}$ cm^{-3} for the interstellar medium and $A_* < 5 \times 10^{-4}$ for wind). These predictions can be tested using the afterglow observations from current and upcoming radio facilities such as the Karl G. Jansky Very Large Array, the Low-Frequency Array, the Five Hundred Meter Aperture Spherical Telescope, and the Square Kilometer Array.

Key words: gamma-ray burst: general – radiation mechanisms: non-thermal

1. INTRODUCTION

Even decades after their discovery, the central engine of gamma-ray bursts (GRBs) and the way it powers the explosion still remain largely unsolved (Kumar & Zhang 2015). The nature of the outflow from the central engine, mainly its composition and degree of magnetization, are still not properly understood. The prompt and early multi-wavelength emission is the main messenger used to probe the central engine. Early X-ray emission is known to display emission components like flares and "internal plateaus," which are usually ascribed to late central engine activities (Nousek et al. 2006; Zhang et al. 2006; Troja et al. 2007). Early multi-wavelength emission should also contain the emission from the reverse shock (RS) that develops once the ejecta encounter the cold medium surrounding the burst (Mészáros & Rees 1997, 1999; Sari & Piran 1999a, 1999b). A strong RS is developed if the outflow from the central engine is baryonic, i.e., the magnetization parameter $\sigma \leqslant 0.1$.[3] Because the ejecta densities are higher compared to that of the ambient medium, the RS temperature is lower, leading most of its emission toward frequencies around and lower than the optical band.

Thanks to the abundant observational data in the optical band, most of the studies of RS emission in the literature so far have focused on the optical/IR band (e.g., Mészáros & Rees 1999; Sari & Piran 1999b; Kobayashi & Zhang 2002, 2003; Kumar & Panaitescu 2003; Zhang et al. 2003; Wu et al. 2003; Fan et al. 2004; Nakar & Piran 2004; Zhang & Kobayashi 2005; Zou et al. 2005; Jin & Fan 2007; Harrison & Kobayashi 2013; Japelj et al. 2014; Gao et al. 2015), see the

recent review by Gao & Mészáros (2015). Due to the improved sensitivity of the Karl G. Jansky Very Large Array (JVLA), deep and fast monitoring campaigns of radio afterglows are now possible (Chandra & Frail 2012; Laskar et al. 2013). Lower frequency studies are possible with the Low-Frequency Array (LOFAR) and in the future with the Five Hundred Meter Aperture Spherical Telescope (FAST), and the Square Kilometer Array (SKA). In particular, the SKA will dramatically improve radio afterglow detection rates or lower the upper limits. A detailed theoretical study of RS radio emission predictions is called for.

Sari & Piran (1995) and Kobayashi (2000) derived the thermodynamical parameters of the RS for a constant-density external ambient medium and estimated the synchrotron emissivity. Later, several authors (Kobayashi & Zhang 2003; Wu et al. 2003; Kobayashi et al. 2004; Zou et al. 2005) extended the formalism to an ambient medium driven by a stellar wind. Recently, Gao et al. (2013a) presented a consolidated review of analytical expressions for RS flux evolution. The difficulty of studying radio RS emission properties lies in correctly accounting for the synchrotron self-absorption effect in many different spectral regimes. Several authors have in the past incorporated self-absorption in the reverse shocked ejecta (Kobayashi & Zhang 2003; Nakar & Piran 2004; Zou et al. 2005). In particular, Gao et al. (2013a) presented a detailed treatment of self-absorption in all possible spectral regimes for both RS and forward shock (FS) emission. In most previous treatments, many authors have assumed the RS microphysics to be the same as that of the FS for the sake of reducing the number of parameters. However, since the upstream of the RS is the ejecta from the central engine, which can be very different from the upstream of the FS, i.e., the circumburst medium, it is possible or even likely that the microphysics parameters of the RSs and FSs are different. In

---

[3] When σ increases further, a RS gradually becomes weaker due to the enhancement of the magnetic pressure in the outflow, and disappears completely at $\sigma > 1$ when the magnetic pressure in the outflow exceeds the FS thermal pressure (Zhang & Kobayashi 2005; Mimica et al. 2009; Mizuno et al. 2009).

particular, since most central engine models invoke a strong magnetic field at the engine, the magnetization parameter of the RS may be very different from that of the FS. Zhang et al. (2003) found that in order to reproduce bright GRB 990123-like RS emission in the optical band characterized by a $\sim t^{-2}$ decay, the RS should be more magnetized than the FS. Zhang & Kobayashi (2005) investigated the optical RS emission for an arbitrary magnetization parameter σ, and found that a moderately magnetized RS (with σ slightly below unity) can have magnetic fields strong enough to enhance the RS emission but not strong enough to suppress RS dynamics, which is most favorable for RS detection in the optical band. Follow-up studies suggest that a moderately magnetized RS is required to interpret a good fraction of GRBs (e.g., Gomboc et al. 2008; Harrison & Kobayashi 2013; Japelj et al. 2014; Gao et al. 2015). Here we present a comprehensive study of low-frequency RS emission in both constant-density and wind-driven ambient medium profiles with the self-absorption processes fully taken into account. We will examine the variation in light curve depending on the microphysics of the reverse shocked medium, in particular, the consequence of a moderately magnetized RS.

In Section 2 we discuss the basic framework of the external FS–RS model, and introduce the main parameters of the problem. In Section 3, we describe the estimation of the synchrotron self-absorption frequency. Sample light curve with varying parameters are presented in Section 4. The conditions for detectable RS emission are presented in Section 5. The results are summarized in Section 6 with a discussion.

2. RS EMISSION

GRBs are explosions powered by a central engine which is believed to launch a collimated outflow of ultra-relativistic ejecta. When the ejecta encounter the circumburst medium, a two-shock system develops. A FS moves into the circumburst medium and a RS propagates back into the ejecta. The RS starts off as Newtonian and becomes relativistic if the ejecta are thick enough. In the standard framework, the RS dynamics is considered in two asymptotic regimes: the Newtonian (thin shell) and the relativistic (thick shell) (Sari & Piran 1995, hereafter SP95), (Kobayashi 2000; hereafter K00). A critical condition is whether the blast wave accumulates a mass of M_{ej}/η (where M_{ej} is the total ejected mass in the shell and η is the initial Lorentz factor of the ejecta) before the RS becomes relativistic. This can be translated to a comparison between the time (t_γ) it takes for the FS to accumulate M_{ej}/η mass and the duration of the burst itself (T), i.e., $t_\gamma > T$ for a non-relativistic RS (or thin shell) and $T > t_\gamma$ for a relativistic RS (or thick shell). The shock-crossing time can, in general, be written as $t_\times = \max(t_\gamma, T)$. See SP95 and K00 for detailed discussions of these timescales.

Once the RS–FS system has developed, four distinct regions can be defined. Region-1 is the unshocked ambient medium, Region-2 is the forward shocked shell, Region-3 is the reverse shocked ejecta, and Region-4 is the unshocked ejected shell. The fundamental parameters characterizing the RS dynamics are (i) the ratio $f(r)$ between the ejected shell density $n_4(r)$ and the ambient medium density $n_1(r)$,

$$f(r) = n_4(r)/n_1(r), \qquad (1)$$

(ii) the initial bulk Lorentz factor η, and (iii) the thickness Δ_0 of the ejected shell, which is related to the observed burst duration T as $\Delta_0 = cT/(1+z)$ where z is the redshift of the burst.

However, $f(r)$ can be written in terms of the total kinetic energy E, external medium density $n_1(r)$, and Δ_0, parameters that are directly related to prompt and FS emission. For this purpose we first rewrite $n_4(r)$ in terms of the ejected mass M_{ej}. $M_{\mathrm{ej}} = 4\pi r^2 \tilde{\Delta} n_4(r)$, where $\tilde{\Delta}$ is the shell thickness in the co-moving frame of the unshocked shell (and is related to the observer frame thickness Δ_0 as $\tilde{\Delta} = \Delta_0 \eta$). For a thick shell one assumes that the shell thickness remains constant throughout or, in other words, the shell does not spread (K00). In the case of a thin shell, the shell spreads as $\Delta(r) = r/\eta^2$.

To rewrite M_{ej} in terms of E and $n_1(r)$, it is convenient to introduce the Sedov length (l). The Sedov length is the radius of the fireball when the rest energy $m(l)c^2$ of the material that is swept up equals the total energy E of the ejecta. Total swept up mass $m(l)$ at l can be written as

$$m(l) = \begin{cases} (4\pi/3)l^3 n_0 m_p & \text{interstellar medium (ISM)}, \\ 4\pi l r_0^2 n_0 m_p & \text{wind}, \end{cases} \qquad (2)$$

where n_0 is used to rewrite $n_1(r)$. For a constant-density ambient medium, $n_0 = n_1/(1\mathrm{atom/cc})$. The wind-driven ambient medium is assumed to be of a density structure $n_1(r) = n_0 (r/r_0)^{-2}$. In terms of the usual parametrization of the wind density profile by Chevalier & Li (1999), $n_0 = 5 \times 10^{11}(A_\star/m_p)r_0^{-2}$, where $A_\star$ of unity corresponds to the density of the medium formed due to a constant mass loss rate of $10^{-5} M_\odot\,\mathrm{yr}^{-1}$, driven by a wind of $1000\,\mathrm{km s}^{-1}$ velocity. From Equation (2), one has

$$l = \begin{cases} (3E/(4\pi n_0 m_p c^2))^{1/3} & \text{ISM}, \\ E/(4\pi r_0^2 n_0 m_p c^2) & \text{wind}. \end{cases} \qquad (3)$$

We now use the fact that M_{ej} is also equal to $E/\eta c^2$, i.e., $m(l)/\eta$, and obtain f as a function of r by equating M_{ej} with $m(l)/\eta$.

$$f(r) = \begin{cases} (l/r)^3 & \text{thin ISM}, \\ l^3/\Delta_0\eta^3 r^2 & \text{thick ISM}, \\ l/r & \text{thin wind}, \\ l/\Delta_0\eta^2 & \text{thick wind}. \end{cases} \qquad (4)$$

Here $f(r)$ is defined before the shock-crossing time ($t_\times$) (i.e., until the unshocked ejecta diminish). It is important to note that for thin shell cases f does not depend on Δ_0 after the shell starts to spread. In other words, in the basic equations of Newtonian RS, the initial shell width Δ_0 does not enter. For a relativistic RS (thick shell) in a wind-driven ambient medium, $f(r)$ is a constant as both n_4 and n_1 depend on r in the same way.

We use $f(t_\times) = f(r = r_\times)$, for normalization: i.e., $f(t_\times) = \eta^2$ for the thin shell for both types of ambient medium, and $f(t_\times) = \eta^{-2}(l/\Delta_0)^{3/2}$ for the thick shell ISM and $f(t_\times) = l/(\Delta_0\eta^2)$ for the thick shell wind.

In order to estimate the synchrotron emission from the reverse shocked region, we need the number density (n_3), energy density (e_3), total number of radiation electrons (N_e), and bulk Lorentz factor Γ_{31} of the shocked region. All these can be obtained once $f(r)$ is known. Next, we derive these quantities in two phases: before and after shock crossing.

2.1. Before Shock Crossing ($t \leqslant t_\times$)

The jump conditions at the FS and the RS place a constraint on $f(r)$ in terms of the Lorentz factors of the shocked medium (see SP95 for detailed expressions of the shock jump conditions). Assuming pressure equilibrium at the contact discontinuity between the shocks, which is valid as long as the shock crossing is fast,[4] we obtain,

$$f = \frac{4\Gamma_{21}^2(\hat{\gamma}-1)}{(\hat{\gamma}\gamma_{34}+1)(\gamma_{34}-1)}, \tag{5}$$

where Γ_{21}, the bulk Lorentz factor of the shocked ambient medium, is assumed to be much greater than unity; γ_{34} is the bulk Lorentz factor of the reverse shocked ejecta with respect to the unshocked ejecta; $\hat{\gamma}$ is the ratio of specific heats of the shocked downstream and varies from $5/3$ for non-relativistic temperatures to $4/3$ for relativistic temperatures. The general expression for $\hat{\gamma}$ is given as (Uhm (2011) and references therein),

$$\hat{\gamma} = \frac{4\gamma_{34}+1}{3\gamma_{34}}. \tag{6}$$

In writing Equation (5), we have assumed that the bulk Lorentz factor of shocked ejecta (Γ_{31}) is equal to Γ_{21}. Γ_{21} is related to η and γ_{34} by

$$\Gamma_{21} = \eta(\gamma_{34} - \sqrt{\gamma_{34}^2 - 1}). \tag{7}$$

This expression has been derived using a Lorentz transformation of velocities and by assuming $\eta \gg 1$.

From Equations (5) and (7), γ_{34} and Γ_{21} can be derived numerically in terms of f and η (Nakar & Piran 2004). However, in our calculations we use the approximate solutions for γ_{34} and Γ_{21} derived by SP95. For the thick shell case, one has

$$\gamma_{34} = \sqrt{\frac{\eta}{2}}\frac{1}{f^{1/4}}, \tag{8}$$

and

$$\Gamma_{21} = \Gamma_{31} = \sqrt{\frac{\eta}{2}}f^{1/4}. \tag{9}$$

For the thin shell, one has

$$\gamma_{34} = 1 + \frac{\eta^2}{f}, \tag{10}$$

and

$$\Gamma_{21} = \Gamma_{31} = \eta\left(1 - \sqrt{\frac{\eta^2}{2f}}\right). \tag{11}$$

We can now obtain the number density $n_3 = 4\gamma_{34}n_4$ and the thermal energy density $e_3 = (\gamma_{34}-1)n_3 m_p c^2$ of the shocked ejecta in terms of η, $f(r)$ and Γ_{31}.

For the total number of shocked electrons, the only remaining parameter required to estimate the synchrotron flux,

one has (K00)

$$N_e = N_\times \frac{t}{t_x}, \tag{12}$$

for the thick shell (both wind and ISM),

$$N_e = N_\times\left(\frac{t}{t_x}\right)^{1/2}, \tag{13}$$

for thin shell wind, and

$$N_e = N_\times\left(\frac{t}{t_x}\right)^{3/2}, \tag{14}$$

for the thin shell ISM. In the above equations, $N_\times = E/(\eta m_p c^2)$ is the number of shocked electrons at $t_\times$ and $t = r/(2\Gamma_{31}^2 c)$ is the observer time.

2.2. After Shock Crossing ($t > t_\times$)

Analytical treatments of the evolution of the RS medium after shock crossing are heavily approximated. One assumption that is often used, which we follow here, is that after shock crossing the reverse shocked ejecta achieve the Blandford–McKee (BM) profile (Kobayashi 2000; Kobayashi & Sari 2000). For the relativistic RS this leads to $\Gamma_{31} \propto r^{-7/2}$, where k is the radial profile index of the ambient medium ($k = 2$ for wind and $k = 0$ for the ISM). Kobayashi & Sari (2000) noticed that for the non-relativistic RS, Γ_{31} does not need to follow the BM profile. Instead it follows $\Gamma_{31} \propto r^{-g}$, where g takes a range of values, e.g., $3/2 < g < 7/2$ for the ISM (Kobayashi & Sari 2000). Nevertheless, as mentioned in Kobayashi & Sari (2000), this range in g does not give rise to a large range in the temporal index of the flux.

The remaining assumption is about the thermodynamics of the reverse shocked ejecta. For a relativistic RS we assume that the sound speed $c_s \sim c/\sqrt{3}$, since protons become relativistic. Since the co-moving width (Δ') of the shock increases as $c_s r/(\Gamma_{31}c)$, the number density scales as $n_3 = N_e/(4\pi r^2\Delta') \propto \Gamma_{31}/r^3$. For a non-relativistic RS, protons need not be relativistic, hence we consider $c_s \sim \sqrt{p_3/\rho_3}$, where p_3 is the pressure and ρ_3 the mass density of the reverse shocked ejecta. Assuming an adiabatic equation of state, $p_3 \propto n_3^{\hat{\gamma}}$, we can obtain both n_3 and p_3. Once p_3 is known, e_3 can be obtained as $e_3 = p_3(\hat{\gamma}-1)$. Using pre-shock-crossing relations (Section 2.1) to normalize n_3 and e_3 at $t_\times$, we obtain,

$$n_3 = n_3(t_\times)\left(\frac{r}{r_\times}\right)^{-6(3+g)/7}$$
$$e_3 = e_3(t_\times)\left(\frac{r}{r_\times}\right)^{-8(3+g)/7}, \tag{15}$$

for the thin shell. We have used $g = 2$ for the ISM and $g = 1$ for wind, and $r_\times = r(t = t_\times)$. For the thick shell, one has

$$n_3 = n_3(t_\times)\left(\frac{r}{r_\times}\right)^{3+k-7/2}$$
$$e_3 = e_3(t_\times)\left(\frac{n_3}{n_3(t_\times)}\right)^{4/3}, \tag{16}$$

The number of shocked electrons N_e remains the same as $N_\times$ for $t > t_\times$ in all cases. We refer to K00 for a detailed description

---

[4] This assumption becomes a bad approximation if the RS is long-lived (Beloborodov & Uhm 2006; Uhm 2011).

of the uncertainties involved in the dynamics and thermo-dynamics of Region-3 post-shock-crossing.

2.3. Microphysics of RS and Synchrotron Spectrum

Once we know n_3, e_3, N_e, and Γ_{31}, we can calculate synchrotron emission from the RS at any given time provided we also know the microphysics of the shocked region that decides the energy content in magnetic fields and electrons. We follow the standard approach in which magnetic fields and electrons in the shocked medium are assumed to carry a constant fraction of the post-shock thermal energy density. The co-moving magnetic field strength in the shocked medium is $B = \sqrt{8\pi\epsilon_{B,RS}e_3}$, where $\epsilon_{B,RS}$ is the fractional energy content in the magnetic field. Energy density u_e in non-thermal electrons is, $u_e = \epsilon_e e_3$. In order to quantify the differences of microphysics parameters in the two shocked regions, we define the ratios[5]

$$\mathcal{R}_e = \frac{\epsilon_{e,RS}}{\epsilon_{e,FS}},$$

$$\mathcal{R}_B = \frac{\epsilon_{B,RS}}{\epsilon_{B,FS}}. \qquad (17)$$

Assuming the electrons are distributed as a power-law in energy with index p, which we take to be the same as that of the FS, the minimum Lorentz factor of the electron distribution can be derived as $\gamma_m = \epsilon_{e,RS}\frac{p-2}{p-1}\frac{e_3}{n_3 m_e c^2}$.

The cooling break γ_c in the electron spectrum before shock crossing is $\frac{6\pi m_e c}{\sigma_T}\frac{1}{2B^2\Gamma_{31}t}$ (Sari et al. 1998). After shock crossing, γ_c becomes a cut-off Lorentz factor since no new electrons are added, and follows the same temporal evolution as γ_m (Wu et al. 2003).

The synchrotron spectral parameters ν_m and ν_c are derived from γ_m and γ_c, respectively, using the expression $\nu_{m,c}(\gamma_e) = \frac{e}{2\pi m_e c}B\gamma_{m,c}^2\Gamma_{31}$. The peak flux f_m (at ν_m for slow cooling and at ν_c for fast cooling) is $f_m = \frac{\sqrt{3}e^3}{m_e c^2}B\frac{N_e\Gamma_{31}}{4\pi d_L^2}$ (Wijers & Galama 1999). For the FS, the same expressions hold for $\nu_{m,c}$ and f_m with Γ_{31} replaced by Γ_{21}. The synchrotron spectrum f_ν is assumed to be a combination of broken power-laws with index $1/3$ for $\nu < \nu_m$, $-(p-1)/2$ for $\nu_m < \nu < \nu_c$, $-1/2$ for $\nu_c < \nu < \nu_m$, and $-p/2$ for $\max(\nu_m, \nu_c) < \nu$. In the numerical calculations, we introduce a smoothing to the spectral breaks.

3. ESTIMATION OF SYNCHROTRON SELF-ABSORPTION FREQUENCY

The synchrotron spectrum described in the previous section is optically thin. However, due to self-absorption, the spectrum is expected to be modified in the low-frequency regime. We derive the self-absorption frequency using two different methods: the optical-depth method and the blackbody method (see below). Comparing the extent of absorption in the RS and FS medium, we see that the RS self-absorption frequency is much higher than that of the FS.

3.1. Optical-depth Method

The optical depth $\tau_\nu = \alpha'_{\nu'}\Delta'$ and self-absorption frequency ν_a corresponds to $\tau_\nu = 1$. We obtain ν_a by solving for τ_ν using $\alpha'_{\nu'}$ from Rybicki & Lightman (1979) and $\Delta' = N_e/(4\pi n_3 r^2)$.

We normalize the frequency variation of τ_ν in terms of τ_{ν_p} (τ_{ν_m} for slow cooling and τ_{ν_c} for fast cooling), the optical depth at ν_p (ν_m for slow cooling and ν_c for fast cooling). This gives

$$\tau_\nu/\tau_{\nu_p} = \begin{cases} (\nu/\nu_p)^{-5/3}, & \nu < \nu_p, \\ (\nu/\nu_p)^{-(p+4)/2}, & \nu_p < \nu < \nu_\star, \\ (\nu_\star/\nu_p)^{-(p+4)/2}(\nu/\nu_\star)^{-(p+5)/2}, & \nu_\star < \nu, \end{cases}$$

where $\nu_\star = \max(\nu_m, \nu_c)$.

Hence ν_a can be expressed as,

$$\nu_a = \begin{cases} \nu_p\,\tau_{\nu_p}^{3/5}, & \nu_a < \nu_p \\ \nu_p\,\tau_{\nu_p}^{\frac{2}{p+4}}, & \nu_p < \nu_a < \nu_\star \\ \nu_p\,\tau_{\nu_p}^{\frac{2}{p+5}}\left(\frac{\nu_p}{\nu_\star}\right)^{\frac{p+4}{p+5}}, & \nu_\star < \nu_a. \end{cases} \qquad (18)$$

3.1.1. Comparison of Self-absorption between FS and RS

For the reverse shocked medium, τ_{ν_p} can be written as,

$$\tau_{\nu_p}(RS) = \frac{\sqrt{3}}{8}\,3^{p/2}\Gamma[(3p+2)/12]\Gamma[(3p+22)/12]$$
$$\times\,e\frac{N_e}{r^2}(p-1)\gamma_p^{-5}B^{-1}. \qquad (19)$$

where $\Gamma[Z]$ is the Euler Gamma function. Similarly, the optical depth estimated for the FS gives

$$\tau_{\nu_p}(FS) = 2\sqrt{3}\,\pi 3^{p/2}\Gamma[(3p+2)/12]\Gamma[(3p+22)/12]$$
$$\times\,en_1(r)\frac{r}{a}(p-1)\gamma_p^{-5}B^{-1}. \qquad (20)$$

Here we have assumed the co-moving frame thickness of the downstream of the FS to be $r/(a\Gamma_{21})$, where a is a numerical factor of the order of 10. The number density of the upstream medium, $n_1(r)$, is rewritten for wind and the ISM as explained in Section 2.

In order to compare the extent of self-absorption in the FS and RS spectra, we introduce $\mathcal{R}_\tau$, the ratio of the optical depths of the RS and FS at their corresponding peak frequency $\nu_p(t_\times)$ at the shock-crossing time $t_\times$, i.e.,

$$\mathcal{R}_\tau = \frac{\tau_{RS}(t_\times)}{\tau_{FS}(t_\times)} = \frac{1}{4}a\frac{N_e}{4\pi r_\times^3 n_0(r_\times)}\left(\frac{\gamma_m^{RS}}{\gamma_m^{FS}}\right)^{-5}\left(\frac{B^{RS}}{B^{FS}}\right)^{-1}, \qquad (21)$$

where $r_\times$ is the radius of the fireball at shock crossing. The γ_m-ratio and B-ratio between RS and FS depend on $\mathcal{R}_e$ and $\mathcal{R}_B$, respectively, as well as e_3/e_2 and n_3/n_2. Assuming pressure equilibrium implies $e_3/e_2 = 1$. In the following, we use approximate expressions for n_3/n_2 to obtain a rough estimate of $\mathcal{R}_\tau$. These approximations are not used in the code for calculating the light curve.

For a thin shell, one has $n_3/n_2 \sim \eta$ and $M_{ej} = \eta m(t_\times) \sim \eta 4\pi r_\times^3 n_0(r_\times) \sim 3N_e$. Hence $\mathcal{R}_\tau$ for the thin shell for both the

---

ISM and wind profiles is

$$\mathcal{R}_\tau \sim \eta^6 \, \mathcal{R}_e^{-5} \mathcal{R}_B^{-1/2}. \tag{22}$$

For a thick shell, one has $N_e/(4\pi n_0(r_\times) r_\times^3) \sim \Gamma_{31}^2(t_\times)/\eta$ for both types of ambient media. Since the shock is relativistic, one has $n_3(t_\times)/n_2(t_\times) = \gamma_{34}(t_\times) f(t_\times)/\Gamma_{21}(t_\times)$. After employing the relations given in Section 2 for the Lorentz factors and f at $t_\times$, this reduces to $\Gamma_{31}^2(t_\times)/\eta$ for both types of ambient media except minor differences in the numerical factors. Hence, for thick shell, we can write $\mathcal{R}_\tau$ as,

$$\mathcal{R}_\tau = (\Gamma_{31}^2(t_\times)/\eta)^6 \, \mathcal{R}_e^{-5} \mathcal{R}_B^{-1/2}. \tag{23}$$

From Equation (9) it follows that $\Gamma_{31}(t_\times) < \sqrt{\eta}$, consequently, $\mathcal{R}_\tau$ is lower for thick shells than for thin shells for the same values of η, $\mathcal{R}_e$ and $\mathcal{R}_B$. However, for both thin and thick shells, the denser RS materials are much more optically thick than the FS materials, as expected.

3.2. Blackbody Method

In another widely used method, the self-absorption frequency is determined by equating the blackbody flux with the synchrotron flux (Sari & Piran 1999b; Kobayashi & Zhang 2003). More specifically, here the synchrotron surface flux (F_a') in the co-moving frame at ν_a' is equated to the flux of a blackbody at temperature T in the Rayleigh–Jeans regime. The temperature T is assumed to be max $(\gamma_a, \gamma_m) \times m_e c^2/k_B$, where γ_a is the Lorentz factor of an electron radiating with typical synchrotron frequency ν_a'.

For illustration, we only consider the case $\nu_a < \nu_m < \nu_c$. Using $F_a' = F_m'(\nu_a'/\nu_m')^{1/3}$ and $4\pi d_L^2 f_m \nu_m = 4\pi r^2 \Gamma_{31}^2 F_m' \nu_m'$, we can finally write

$$8\pi \gamma_m m_e c^2 (\nu_a'/c)^2 = f_m \, (d_L/r)^2 \, \frac{1}{\Gamma_{31}} \, (\nu_a'/\nu_m')^{1/3}. \tag{24}$$

The above equation can easily be solved for ν_a for the various RS dynamics and ambient media we considered earlier. The ν_a thus obtained differs from the ν_a derived using the optical-depth method by a factor of $3^{0.3p} (p-1)^{3/5} \Gamma[(3p+2)/12] \Gamma[(3p+22)/12]$. For $p \sim 2.2$–2.5, the ν_a derived using this method is about one-third of the ν_a derived from the optical-depth method. The difference arises because some p dependent terms are not considered in the blackbody method. This result is in agreement with the findings of Shen & Zhang (2009), who have investigated self-absorption in detail for prompt emission.

In Appendix A, we present the expressions of the RS self-absorption frequency for various spectral regimes and density profiles, both before and after shock crossing.

In the optically thick regime, the synchrotron spectrum is modified as ν^2 for $\nu_a < (\nu_m, \nu_c)$ and $\nu^{5/2}$ for $\nu_a > (\nu_m, \nu_c)$.

3.3. Pile-up of Electrons due to Strong Synchrotron Cooling

In certain parameter regimes, the RS emission in a wind medium can encounter the condition of strong synchrotron cooling ($\nu_c < \nu_a$). Under such a condition, electrons would pile up at a certain energy due to the balance of synchrotron cooling and self-absorption heating, so that the spectrum is modified to have a quasithermal component in the low energy regime (Kobayashi et al. 2004). To obtain an exact description of the electron energy spectrum, full numerical calculations are required (Ghisellini et al. 1997). Gao et al. (2013b) used an analytical approximation of this effect within the context of

synchrotron and the synchrotron self compton (SSC) spectrum of GRB prompt and afterglow emission. In our spectrum and light curve calculations, we adopt this method in the strong cooling regime.

4. RADIO LIGHT CURVE

In this section we compute the radio afterglow light curve for the various cases we have considered so far.

Figures 1–8 are radio light curve in four frequencies: 22 GHz, 5 GHz, 150 MHz, and 50 MHz, denoted by $\nu_{\rm obs}$. We consider the ISM (Figures 1–4) and wind (Figures 5–8) cases, for both thin and thick shells. In order to explore a redshift dependence of the results, for each set of parameters, we calculate the light curve for two characteristic redshifts: $z = 1$ and $z = 5$. We obtain the light curve for the four bands for various values of $\mathcal{R}_e$ and $\mathcal{R}_B$. Other parameters (E_{52}, n_0 or $A_\star$, η, ϵ_e, ϵ_B, θ_j, p, T_{90}) are fixed while ensuring that the thin shell and thick shell conditions are satisfied. For comparison, the FS light curve are plotted as the dashed curves.

A higher $\mathcal{R}_B$ leads to higher values for $f_m^{\rm RS}$, $\nu_a^{\rm RS}$, and $\nu_m^{\rm RS}$, and a much lower value for $\nu_c^{\rm RS}$. Increasing $\mathcal{R}_e$ leads to an increase in $\nu_m^{\rm RS}$ and $\nu_a^{\rm RS}$. RS light curve in GHz range frequencies peak when the fireball becomes optically thin ($\nu_{\rm obs} = \nu_a^{\rm RS}$). Increasing $\nu_a^{\rm RS}$ delays this peak. Hence, as $\mathcal{R}_e$ and $\mathcal{R}_B$ increase, the peak shifts to a later time. Since the RS light curve is in the rising phase before the peak, a delayed peak can potentially lead to a higher RS flux. However, if the FS flux is also rising, a delayed peak need not necessarily lead to a higher dominance of RS over FS, as seen in the ISM light curve. For the wind light curve, where the FS flux is nearly constant over time (due to the specific spectral regime the FS is in), a delayed peak results in a mild dominance of RS over FS. This is in contrast to the optical ranges where a higher $\mathcal{R}_B$ always leads to a high RS flux (Zhang et al. 2003; Zhang & Kobayashi 2005).

In lower radio frequencies (MHz range), the fireball remains optically thick during the peak, and the peak is due to a transition in the effective optical depth. During the fireball evolution, the RS medium eventually becomes optically thin but the FS medium is still optically thick to low-frequency RS photons, leading to a change in the effective optical depth. That is, $\nu_a^{\rm RS} = \nu_a^{\rm FS}$. This transition results in a change in the slope of MHz range light curve from a rising to a falling one, thereby resulting in a peak. This peak is always at a later epoch, often an order of magnitude later than the GHz peaks. By this time, $f_m^{\rm RS}$ would be going down steeply, as opposed to $f_m^{\rm FS}$, which is either constant or varying at a much slower rate. Self-absorption of the flux and the reduction in $f_m^{\rm RS}$ together make RS always negligible compared to FS at lower frequencies.

An achromatic break is seen in the light curve due to the jet edge becoming visible (geometric jet break). The break is noticeable in the falling part of the GHz and in the rising part of the MHz light curve. Regarding the redshift dependency, the higher redshift light curve is fainter, as expected.

5. RS DETECTABILITY FROM RS AND FS FLUX COMPARISON

The RS can be detected if it rises above the FS, which is most likely to happen around the RS peak time. A measure of RS detectability is the ratio χ between RS and FS flux at the
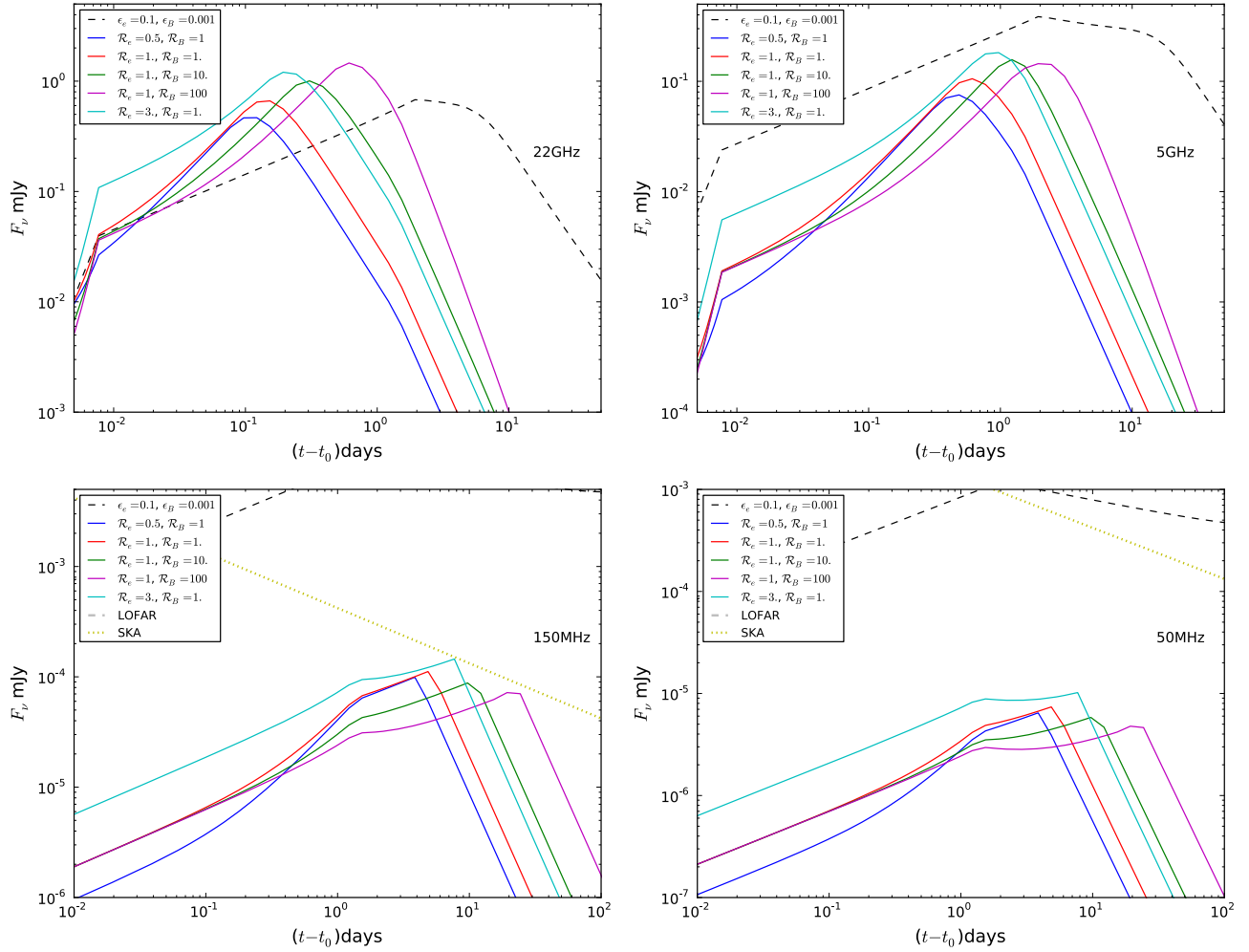
Figure 1. RS and FS light curve for different $\mathcal{R}_e$ and $\mathcal{R}_B$ values in the ISM model. The forward shock light curve is shown as the dashed black curve. The physical parameters are such that the thin shell condition is satisfied : $E_{\mathrm{iso},52} = 5$, $\eta = 100$, and $n_0 = 0.1$. The redshift of the burst is assumed to be $z = 1$. The RS light curve peak times in 22 GHz and 5 GHz correspond to the epochs when the fireball becomes optically thin. For 150 MHz and 50 MHz, the peak times are due to the change in optical thickness of the RS medium (see text). The shock-crossing time is $t_\times \sim 665$ s (0.008 day), the transition due to which can be seen in the 22 GHz light curve. The jet opening angle θ_j is $5°$. An achromatic jet break due to the observer viewing the edge of the jet can be seen at ~1.5 day in the light curve. For the RS, the jet break suppresses the peak flux. For the forward shock, $\epsilon_e = 0.1$ and $\epsilon_B = 0.001$ are used in all figures, and the electron distribution index $p = 2.2$ is used for both FSs and RSs. The RS emission is calculated for a variety of $\mathcal{R}_e$ and $\mathcal{R}_B$ values. The 5σ sensitivity limit of the upcoming SKA radio telescope is shown for 150 MHz. An integration time of $(t - t_0)/3$ and a bandwidth of 50 MHz is used. LOFAR limits are much higher than the expected flux and the SKA limits are higher in 50 MHz.

peak time (t_{peak}) of the RS flux. RS detectability implies

$$\chi = F^{\mathrm{RS}}(\nu_{\mathrm{obs}}, t_{\mathrm{peak}})/F^{\mathrm{FS}}(\nu_{\mathrm{obs}}, t_{\mathrm{peak}}) > 1. \qquad (25)$$

The parameter χ depends on the RS and FS spectral regimes of the observing frequency ν_{obs} at t_{peak}. We now derive some analytical expressions for χ for ν_{obs} in GHz and MHz ranges corresponding to specific combinations of RS and FS spectral regimes. For simplicity, we only consider the more probable slow cooling case in the analytical calculations. We have also performed numerical calculations which can take care of different spectral regimes including fast cooling cases.

5.1. High Radio Frequencies

Following Equation (18), the self-absorption frequency can be written in terms of the optical depth τ_m at ν_m,

$$\nu_a = \nu_m \tau_m^{1/\mu}, \qquad (26)$$

where the index μ is given by

$$\mu = \begin{cases} (p + 4)/2, & \nu_a > \nu_m, \\ 5/3, & \nu_a < \nu_m. \end{cases}$$

In some ranges of the parameters, especially when $\mathcal{R}_B$ is high, the self-absorption frequency can be greater than the cooling frequency. However, this usually happens well past t_{peak}. Therefore we have not considered this case in the analytical calculations. Nevertheless, in the code and in Figures 10–13 this is taken care of (see Section 3.3).

The high radio frequency (GHz range) light curve peaks when the RS medium becomes optically thin to the observed frequency ($\nu_a^{\mathrm{RS}} = \nu_{\mathrm{obs}}$, or $t_{\mathrm{peak}} = t_a$). For typical ranges of physical parameters, the RS spectral breaks at t_a are ordered as $\nu_m^{\mathrm{RS}} < \nu_a^{\mathrm{RS}} < \nu_c^{\mathrm{RS}}$. Using Equation (26), the condition $\nu_m^{\mathrm{RS}} < \nu_a^{\mathrm{RS}}$ can be rewritten as

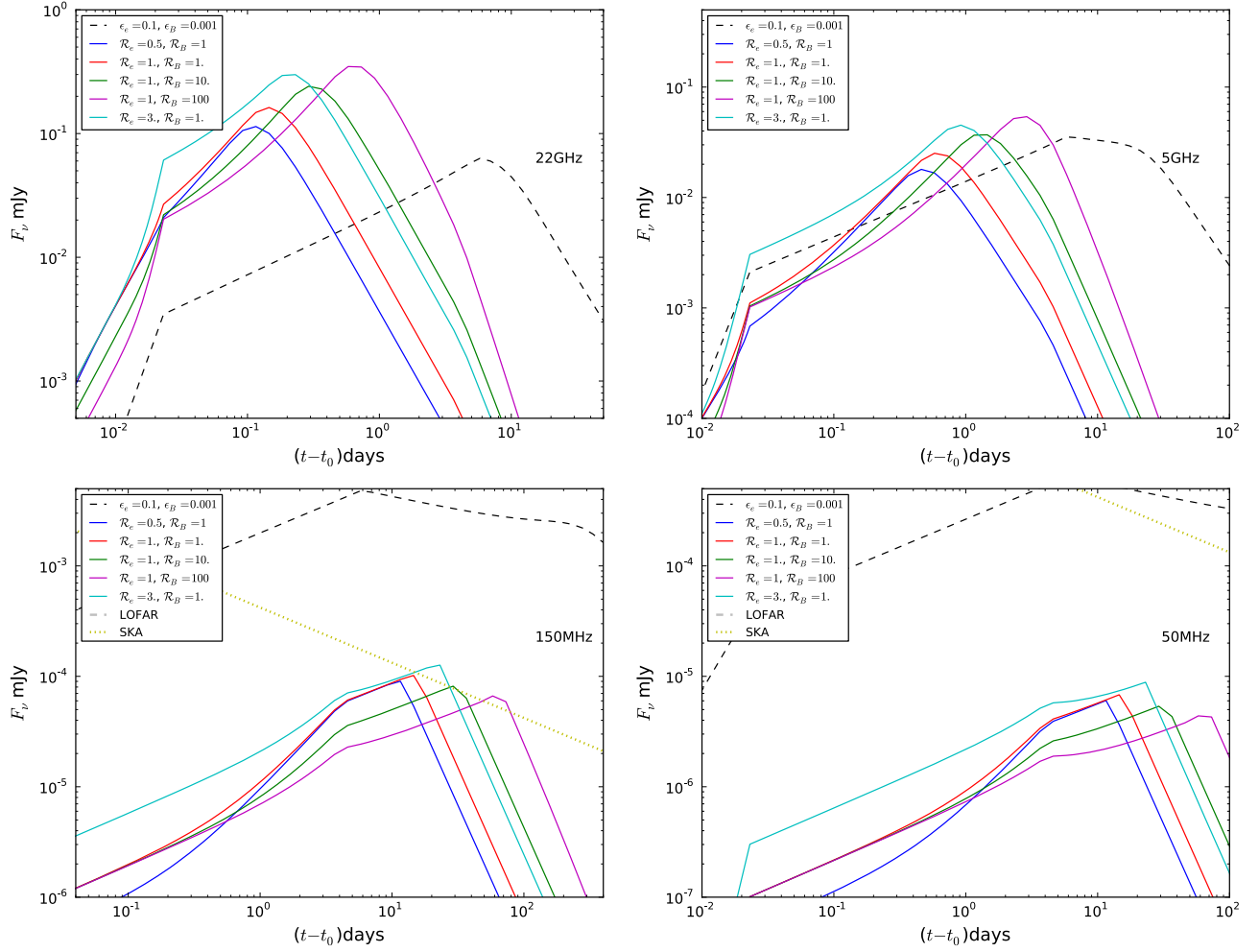$$1 < (\tau_m^{\mathrm{RS}})^{1/\mu}. \qquad (27)$$

Figure 2. The same as previous figure, but for $z = 5$. The shock-crossing time in the observer frame increases to $t_\times \sim 2000$ s (0.02 day) due to time dilation.

To calculate χ, next we consider the FS spectral regime. For standard parameters, the FS spectral breaks at t_a are in the sequence $\nu_a^{FS} < \nu_m^{FS} < \nu_c^{FS}$, with ν_m^{FS} in the THz ranges. That is, $\nu_{obs} < \nu_m^{FS}$. Since $\nu_{obs} = \nu_a^{RS}$ at t_a, we can rewrite this as $\nu_a^{RS} < \nu_m^{FS}$. Substituting Equation (26) for ν_a^{RS}, one obtains

$$(\tau_m^{RS})^{1/\mu} < \nu_m^{FS}/\nu_m^{RS}. \tag{28}$$

Combining the conditions on both the FS and RS spectral regimes,

$$1 < (\tau_m^{RS})^{1/\mu} < \nu_m^{FS}/\nu_m^{RS}. \tag{29}$$

A consequence of the assumptions on the RS and FS spectral regimes is $\nu_a^{FS} < \nu_a^{RS}$, i.e., the RS optical depth is higher than the FS optical depth. We treat the opposite condition in the low-frequency analysis (next section).

Sketches of the RS and FS spectra at t_a are given in Figure 9 (left panel).

Finally, the RS and FS fluxes at t_{peak} can be obtained as,

$$F^{RS}(\nu_{obs}, t_a) = F_m^{RS} \left(\frac{\nu_a^{RS}}{\nu_m^{RS}} \right)^{-\beta}, \tag{30}$$

where $\beta = (p - 1)/2$, and

$$F^{FS}(\nu_{obs}, t_a) = F_m^{FS} \left(\frac{\nu_m^{RS}}{\nu_m^{FS}} \right)^{1/3} \tau_m^{1/3\mu}. \tag{31}$$

5.2. Low Radio Frequencies

For the MHz range radio frequencies, which are relevant to SKA and LOFAR, the RS peak is when the RS optical depth falls below that of the FS, and the FS medium starts to become responsible for the absorption of RS photons ($\nu_a^{RS} = \nu_a^{FS}$ or $t_{peak} = t_{eq}$). When ν_a^{RS} becomes ν_a^{FS}, the light curve index changes from a positive value (rising light curve) to a negative value (falling light curve), resulting in a peak.

We see that the sequence of spectral breaks in both RS and FS remain the same as the previous case. But the observed frequency this time is much lower and is still optically thick ($\nu_{obs} < \nu_a^{RS} = \nu_a^{FS}$), unlike for the previous case. Since $\nu_m^{RS} < \nu_a^{RS}$, the condition $1 < (\tau_m^{RS})^{1/\mu}$ holds in this case too.

Since $\nu_a^{FS} < \nu_m^{FS}$, Equation (26) can be written for the FS as $\nu_a^{FS} = \nu_m^{FS}(\tau_m^{FS})^{3/5}$. Equating this to $\nu_a^{RS} = \nu_m^{RS}(\tau_m^{RS})^{1/\mu}$, the spectral conditions finally lead to,

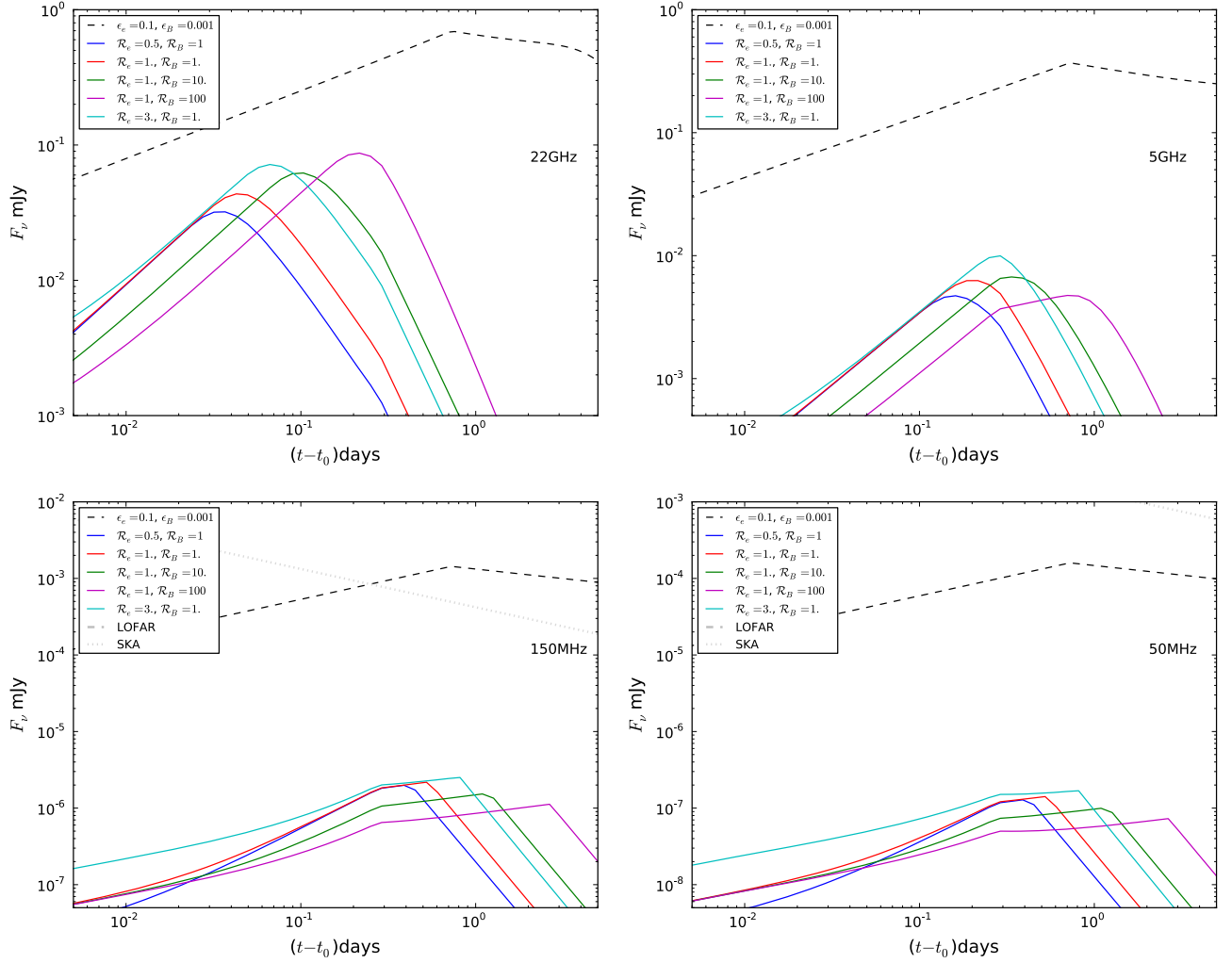$$1 < (\tau_m^{RS})^{1/\mu} = (\tau_m^{FS})^{3/5}(\nu_m^{FS}/\nu_m^{RS}). \tag{32}$$

Figure 3. Light curve for the ISM model, but the physical parameters are such that the thick shell condition is satisfied : $E_{iso,52} = 5$, $\theta_j = 5°$, $\eta = 400$, $n_0 = 1$, and $T = 80$ s, $z = 1$. The additional break before the RS peak in the high $\mathcal{R}_B$ (magenta) case in 5 GHz is the jet break which can be seen more prominently in the rising part of the lower frequency light curve.

Sketches of the RS and FS spectra at t_{eq} are given in Figure 9 (right panel).

In MHz frequencies, RS is not likely to be significant due to the combination of two effects. First, f_m^{RS} is a sharply decreasing function of time as opposed to f_m^{FS} (which, depending on the ambient medium, either stays constant or decays at a slower rate). As t_{eq} is much larger than t_a (of the order of 50 times), the RS spectrum falls well below that of the FS by the time of the RS peak. Second, at t_{eq}, the RS is still optically thick, which further reduces the flux.

It is possible that $t_j < t_{eq}$, but we have not considered such a case in the analytical estimates. Our numerical code, however, takes care of this effect (see Figures 1–8).

Finally, the RS and FS fluxes can be written, respectively, as

$$F^{RS}(\nu_{obs}, t_{eq}) = F_m^{RS} \left(\frac{\nu_a^{RS}}{\nu_m^{RS}} \right)^{-\beta} \left(\frac{\nu_{obs}}{\nu_a^{RS}} \right)^{5/2}, \qquad (33)$$

and

$$F^{FS}(\nu_{obs}, t_{eq}) = F_m^{FS} \left(\frac{\nu_a^{FS}}{\nu_m^{FS}} \right)^{1/3} \left(\frac{\nu_{obs}}{\nu_a^{FS}} \right)^{2}. \qquad (34)$$

Even in the cases where RS is not significant or the RS peak is missing from observations, Equations (29) and (32) can still

provide sufficient insight into the underlying physical parameters if the spectral regime can be inferred.

In Appendix B, we provide the analytical expressions of χ in high and low radio frequencies.

5.3. RS Detectability

We use χ to probe the parameter space to find regions where RS is prominent. For this we employ numerical calculations of χ, where we follow the shock dynamics continuously and hence any change in the spectral regimes is accounted for automatically.

In our analytical calculations of χ we have used approximations for the thermodynamic quantities of the RS downstream. Moreover, we have not considered jet break and spectral smoothing. This has led to some deviation from the numerical values, however, the overall trend (variation with respect to physical parameters) remains the same.

Figures 10–13 display the variation of χ across frequencies. We can see that at lower radio frequencies, the RS becomes insignificant, so we focus our attention on high frequencies.

We notice a strong negative correlation of χ and the ambient medium density. For both the ISM and the wind media, a lower ambient density results in a higher χ. This is in agreement with the findings of Laskar et al. (2013), where a low $A_\star$ value of
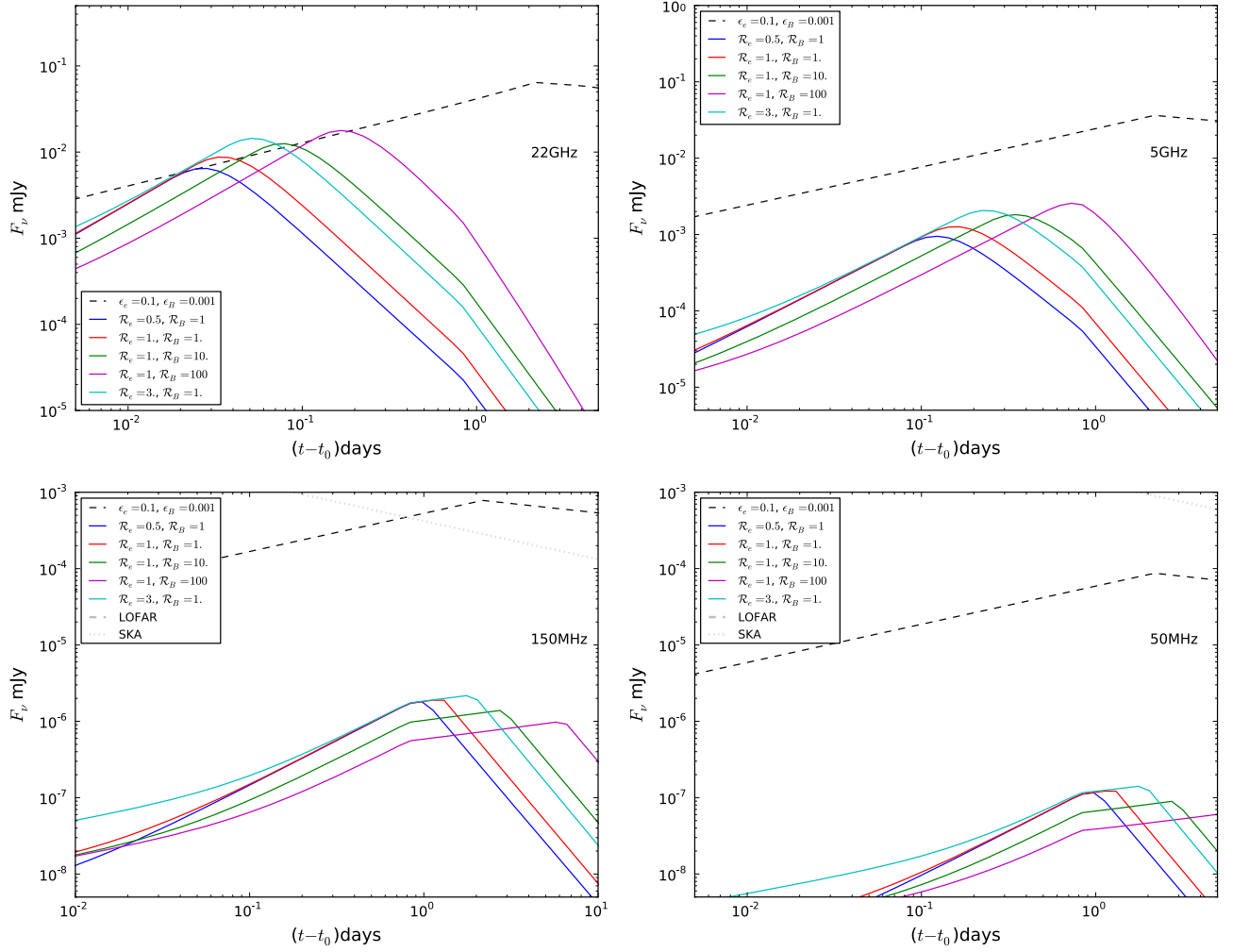
Figure 4. The same as the figure 4, for $z = 5$.

GRB 130427A is needed to produce a bright RS. In any case, for standard microphysics parameters, unless n is extremely low (e.g., $n_0 < 10^{-3}\,\mathrm{cm}^{-3}$ for the ISM or $A_* < 5 \times 10^{-4}$ for wind), the RS component is not supposed to outshine the FS emission in frequencies below ~1 GHz.

Apart from this density dependence, a strong positive correlation is seen between χ and ϵ_e. A higher ϵ_e results in a higher ν_m^{FS}, which for a fixed f_m^{FS} leads to a smaller FS flux in radio ($\nu_{\rm obs} < \nu_m^{FS}$) frequencies. Since the RS is in the spectral regime $\nu_m^{RS} < \nu_{\rm obs} < \nu_a^{RS}$, the RS flux is not as sensitive to ϵ_e as the FS flux, resulting in a higher χ. However, ϵ_e does not seem to vary largely among bursts (Santana et al. 2014; Gao et al. 2015). As we have already seen from the light curve (Section 4), χ depends very weakly on $\mathcal{R}_B$ for both types of ambient media, and the wind model has a slightly stronger dependence on $\mathcal{R}_B$ than the ISM model.

6. SUMMARY AND CONCLUSIONS

In this paper, we apply the previous results of Newtonian and relativistic RS dynamics to obtain radio afterglow light curve for both the constant-density and the wind-driven ambient media. Special attention is paid to a detailed analysis of synchrotron self-absorption from both the RS and the FS regions. Major findings from our investigation can be summarized as follows:

1. Unlike optical/IR light curve which typically peak at the shock-crossing time, the radio RS light curve (in high frequencies, e.g., GHz and above) peak at the epoch when the fireball becomes optically thin to synchrotron emission. Hence, the radio RS peak is delayed with respect those in the optical/IR frequencies, and appears around ~1 day.

2. In the low radio frequency regime, the forward shocked ejecta remain optically thick even when the RS ejecta become optically thin ($\nu_a^{FS} > \nu_a^{RS}$). This sets the effective ν_a to that of the FS and changes the light curve evolution from what has been described previously in the literature. The transition from RS-dominated self-absorption to FS-dominated self-absorption results in a peak in the radio RS light curve at low frequencies (e.g., below MHz).

3. However, due to self-absorption and due to the steep decay of f_m^{RS}, the low-frequency RS light curve always remains well below its FS counterpart.

4. We estimate the ratio (χ) of the forward to RS flux at the peak time of the RS. The RS is detectable when $\chi > 1$. For typical shock microphysics parameters, the RS cannot outshine the FS below 1 GHz ($\chi < 1$), unless the medium density is extremely low (e.g., $n_0 < 10^{-3}\,\mathrm{cm}^{-3}$ for the ISM and $A_* < 5 \times 10^{-4}$ for wind).

5. In the optical frequencies, a higher magnetization has the power to make the optical light curve RS dominating. But
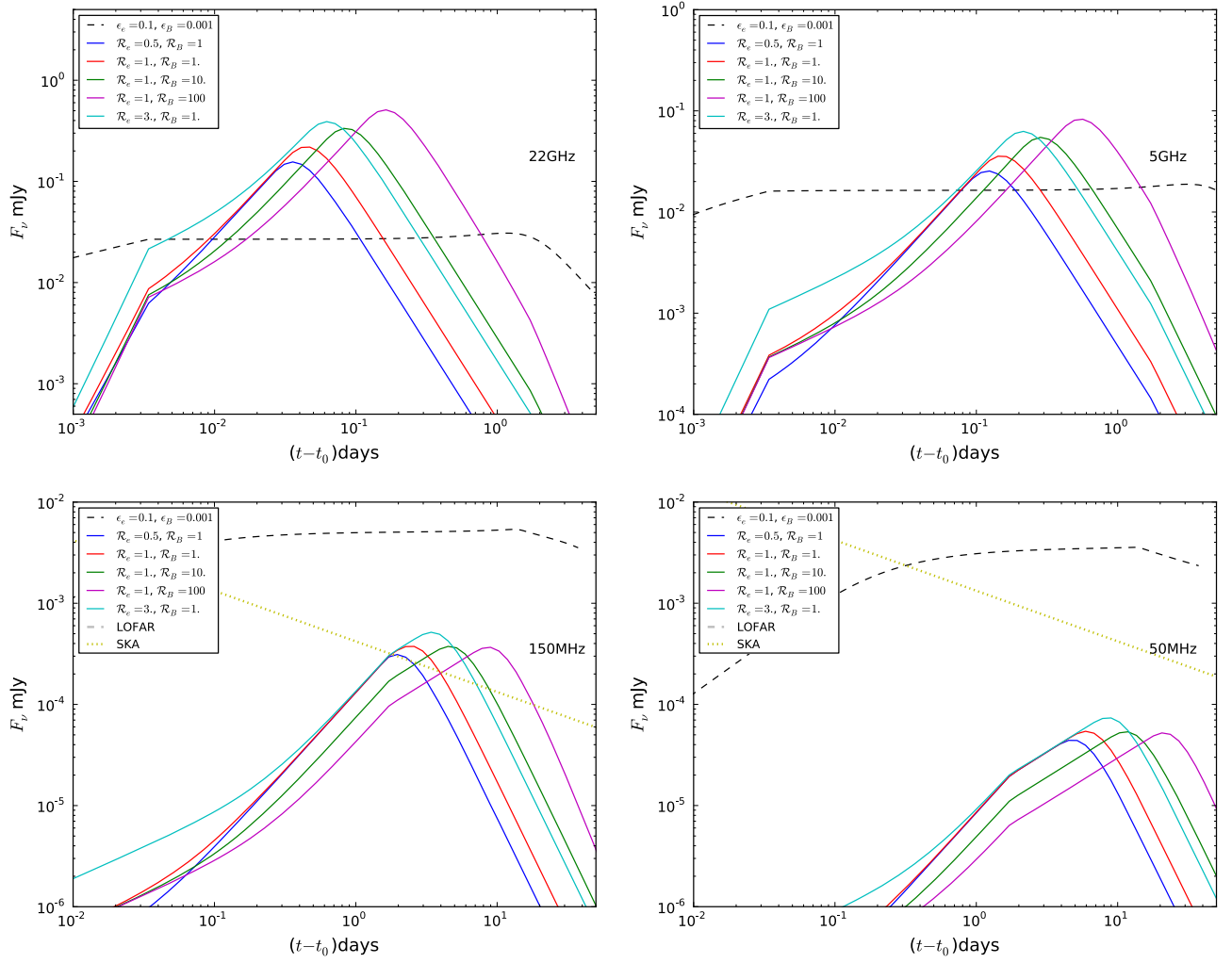
Figure 5. Same as Figure 1 but for the thin shell wind model. Physical parameters are : $E_{\rm iso,52} = 5$, $A_\star = 0.01$, $\eta = 100$, and $z = 1$ which leads to $t_\times = 295$ s (0.003 day). The forward shock flux is nearly constant as both 22 GHz and 5 GHz are between $\nu_a^{\rm FS}$ and $\nu_m^{\rm FS}$. The physical parameters are such that, unlike in the previous figures, the peak time corresponds to the crossing of ν_a through the radio band including lower frequencies.

the radio RS light curve does not necessarily become RS dominant with a higher ejecta magnetization.

6. A lower ambient density or ϵ_e favors RS detectability.

With the improved sensitivity of the JVLA, it is now possible to test the RS models and infer the RS physical parameters with better accuracy, which in turn sheds light on the nature of the ejecta (Laskar et al. 2013; Urata et al. 2014). Melandri et al. (2010), Kopac et al. (2015), etc. have discussed various aspects of radio RS emission. Gao et al. (2013a) have produced a complete reference of analytical RS light curve. Future radio data from JVLA, LOFAR, FAST, and SKA are desired to test the model predictions presented in this work.

APPENDIX A
SYNCHROTRON SELF-ABSORPTION FREQUENCIES

In this appendix, we present expressions for the RS self-absorption frequencies. In cases with explicit numerical

dependence on η, we have normalized η to a typical value of 300 (i.e., $\eta_{300} = \eta/300$). Numerical factors with intricate p dependences are replaced with a best fit function form. The observer time t is in units of seconds. All the parameters are for the RS. For the expressions as a function of the FS microphysics parameters, one can simply replace ϵ_e and $\epsilon_{\rm B}$ by $\mathcal{R}_e \epsilon_{e,\rm FS}$ and $\mathcal{R}_{\rm B} \epsilon_{\rm B,FS}$, respectively. We note that these expressions are consistent with those derived by Gao et al. (2013a) up to a small discrepancy in the coefficients.
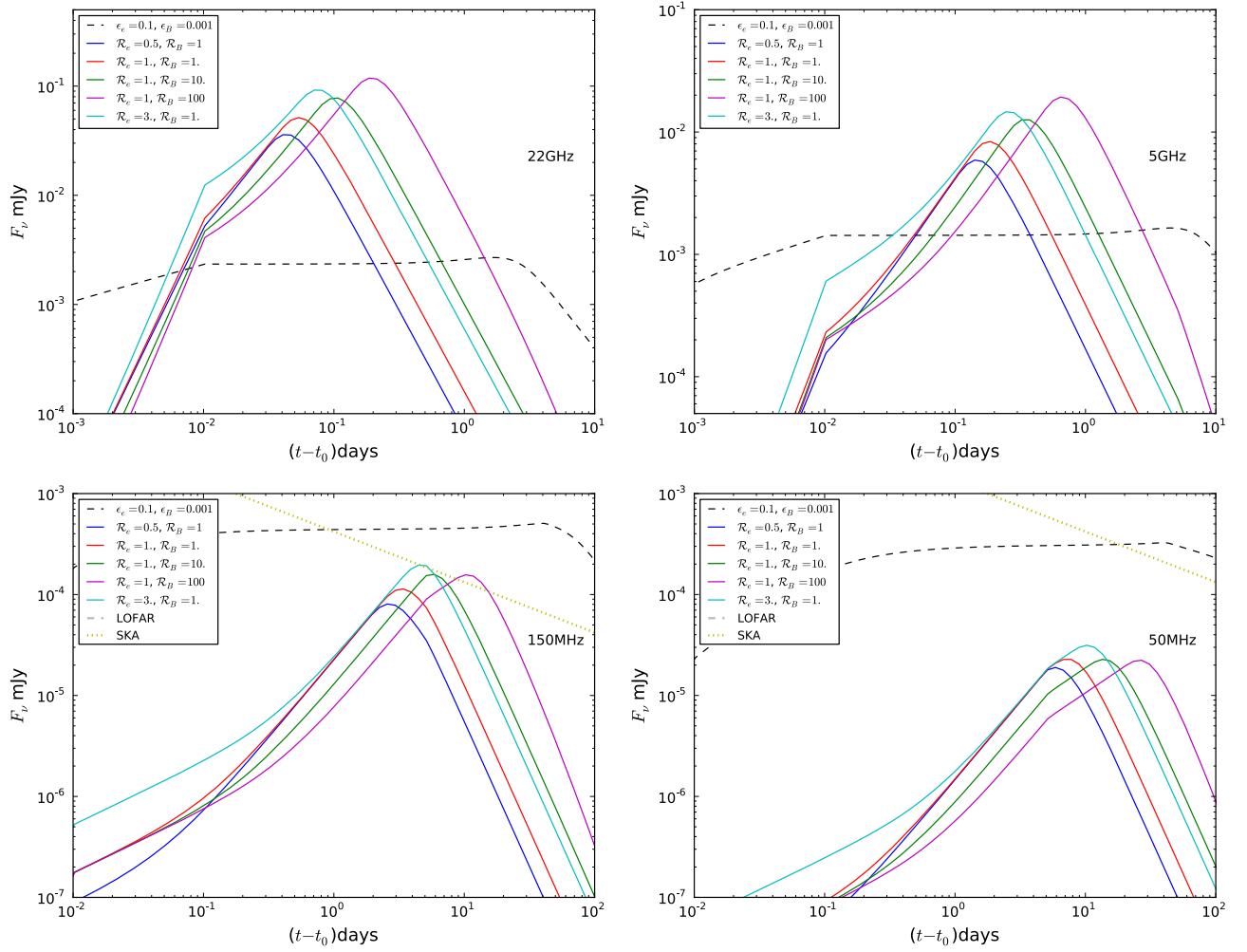
A.1. Thin Shell ISM

Before shock crossing, for $\nu_a < \nu_m < \nu_c$, one has

$$\nu_a = 2.4 \times 10^{14} \text{ Hz } t^{-33/10} \frac{3^{3(p+1)/10}(p-1)^{8/5}}{(p-2)}$$

$$\times \frac{E_{52}^{13/10} \epsilon_{\rm B}^{1/5}}{n_0^{1/2} \epsilon_e \eta_{300}^{36/5}}. \tag{35}$$

For $\nu_m < \nu_a < \nu_c$, one has

$$\nu_a = 1.6 \times 10^{13} \text{ Hz } 10^{-4.7p} t^{\frac{6p-7}{p+4}} E_{52}^{\frac{3-2p}{p+4}} n_0^{\frac{5p}{8+2p}} \eta^{\frac{6(3p-2)}{p+4}} \epsilon_e^{\frac{2(p-1)}{p+4}} \epsilon_{\rm B}^{\frac{p+2}{8+2p}}. \tag{36}$$

Figure 6. The same as figure 5, for $z = 5$.

For $\nu_a < \nu_c < \nu_m$, one has

$$\nu_a = 1.2 \times 10^{15} \text{ Hz } 3^{3(p+1)/10} \, t^{7/10} \, E_{52}^{3/10} n_0^{3/2} \eta_{300}^{19/5} \epsilon_B^{6/5}.$$
(37)

After shock crossing, for $\nu_a < \nu_m < \nu_c$, one obtains

$$\nu_a = 2.6 \times 10^{12} \text{ Hz } t^{-\frac{102}{175}} 3^{\frac{3(p+1)}{10}} \frac{(p-1)^{8/5}}{(p-2)}$$
$$\times \frac{E_{52}^{69/175} n_0^{71/175} \eta^{8/175} \epsilon_B^{1/5}}{\epsilon_e}.$$
(38)

For $\nu_m < \nu_a < \nu_c$, one has

$$\nu_a = 10^{17} \text{ Hz}(24.5p^3 - 145.6p^2 + 305.2p - 222.3)$$
$$\times t^{\frac{-2(52+27p)}{35p+140}} E_{52}^{\frac{18p+58}{35p+140}} n_0^{\frac{94-p}{280+70p}} \eta^{-\frac{44+74p}{35p+140}} \epsilon_e^{\frac{2(p-1)}{p+4}} \epsilon_B^{\frac{p+2}{8+2p}}.$$
(39)

We note that since most indices have p dependences, one cannot obtain the correct numerical coefficient without assuming a p value. Therefore, the numerical values of ν_a expressions cannot be regarded as the typical value. For example, for Equation (39), for $p \sim 2.2$, the exponents of η and ϵ_B are ~ -1 and ~ 0.3, respectively. Taking typical values of η

~ 300 and $\epsilon_B \sim 10^{-3}$, the typical value goes down to $\sim 10^{14}$ Hz. The same applies to the expressions for the wind case (Appendices A.3 and A.4).

A.2. Thick Shell ISM

Before shock crossing, for $\nu_a < \nu_m < \nu_c$, one has

$$\nu_a = 10^{17} \text{ Hz } 3^{3(2+p)/10}(1+z) \frac{(p-1)^{8/5}}{(p-2)}$$
$$\times \frac{E_{52}^{3/5} n_0^{1/5} \epsilon_B^{1/5}}{T_{90}^{3/5} \epsilon_e \eta_{300}^{8/5}} t^{-3/5}.$$
(40)

For $\nu_m < \nu_a < \nu_c$, one has

$$\nu_a = 10^{14} \text{ Hz}(49.1 - 26.5p + 4p^2) \left(\frac{p-2}{p-1}\right)^{\frac{2(p-1)}{p+4}}$$
$$\times (p-1)^{\frac{2}{p+4}} E_{52}^{\frac{2}{p+4}} n_0^{\frac{p+2}{2(p+4)}} \eta^{\frac{2(p-2)}{p+4}}$$
$$\epsilon_e^{\frac{2(p-1)}{p+4}} \epsilon_B^{\frac{p+2}{2(p+4)}} T_{90}^{-\frac{2}{p+4}} (1+z)^{\frac{4}{p+4}} t^{-\frac{2}{p+4}}.$$
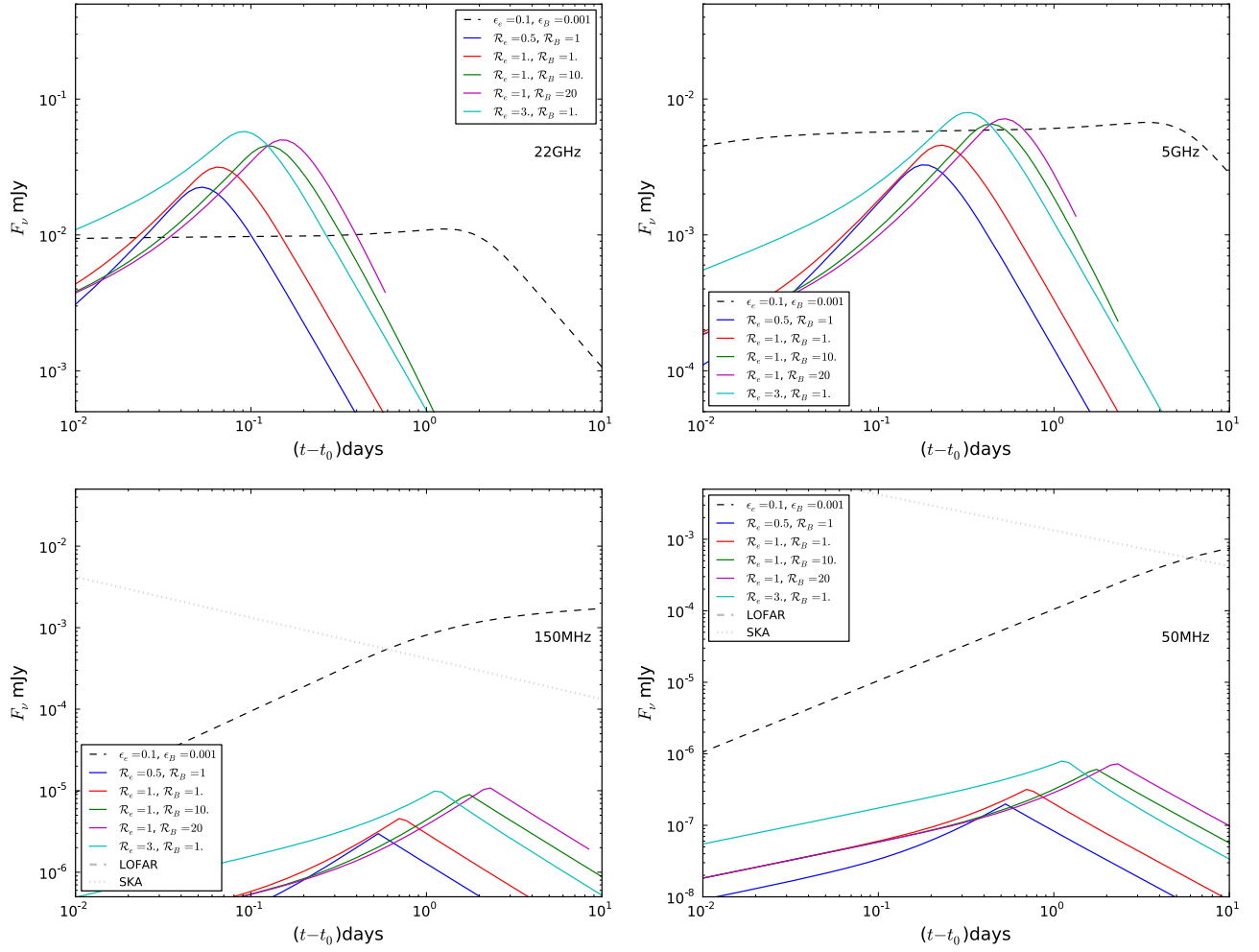(41)

11

Figure 7. The thick shell wind model. The physical parameters are $E_{iso,52} = 5$, $\eta = 300$, $A_\star = 0.01$, and $T = 200$ s. Again, the FS flux is nearly constant for GHz frequencies due to the spectral regime in which the GHz frequency falls. In GHz frequencies, the RS peak corresponds to the fireball becoming optically thin, while for lower frequencies, the peak correspond to change in self-absorption ($\nu_a^{RS} = \nu_a^{FS}$).

For $\nu_a < \nu_c < \nu_m$, one has

$$\nu_a = 6.5 \times 10^{17} \text{ Hz } 3^{0.3(p+1)}$$
$$\times \frac{E_{52}^{17/20} n_0^{19/20} (1+z)^{39/20} \epsilon_B^{6/5}}{T_{90}^{17/20} \eta^{3/5}} \, t^{-0.1}. \quad (42)$$

After shock crossing, for $\nu_a < \nu_m < \nu_c$, one has

$$\nu_a = \frac{4.0 \times 10^{14} \text{ Hz } 3^{0.3(p-9)} (1+z)^{6/5} (p-1)^{8/5} E_{52}^{3/5} n_0^{1/5} \epsilon_B^{1/5}}{(p-2) \eta_{300}^{8/5} T_{90}^{2/3} \epsilon_e}. \quad (43)$$

A.3. Thin Shell Wind

Before shock crossing, for $\nu_a < \nu_m < \nu_c$, one has

$$\nu_a = 3.6 \times 10^{11} \text{ Hz } \frac{3^{\frac{3(p+1)}{10}} (p-1)^{8/5}}{(p-2)}$$
$$\times \frac{(1+z)^{13/10} E_{52}^{13/10} \epsilon_B^{5/2} t^{-23/10}}{\sqrt{A_\star} \epsilon_e \eta_{300}^{26/5}}. \quad (44)$$

For $\nu_m < \nu_a < \nu_c$, one has

$$\nu_a = 2.9 \times 10^{19} 10^{-1.4p} \text{ Hz } \frac{(p-2)^{\frac{2(p-1)}{p+4}} (p-1)^{\frac{12}{p+4}}}{(p-1)^2}$$
$$\times t^{\frac{p-7}{p+4}} (1+z)^{\frac{3-2p}{p+4}} A_\star^{\frac{5p}{2(p+4)}} E_{52}^{\frac{3-2p}{p+4}}$$
$$\epsilon_B^{\frac{p+2}{2(p+4)}} \epsilon_e^{\frac{2(p-1)}{p+4}} \eta^{\frac{4(2p-3)}{p+4}}. \quad (45)$$
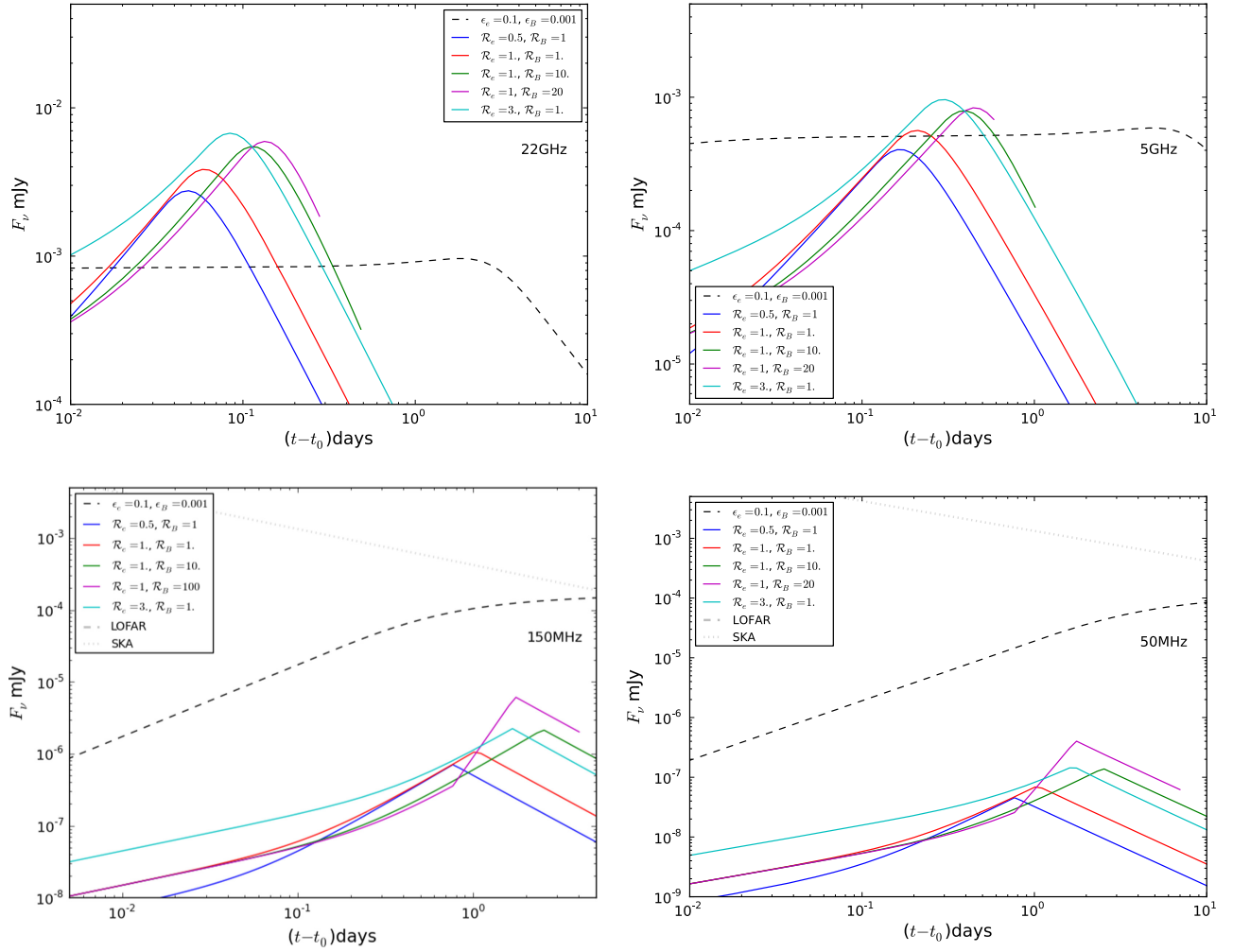
For $\nu_a < \nu_c < \nu_m$, one has

$$\nu_a = \frac{3.3 \times 10^{22} \text{ Hz } A_\star^{3/2} E_{52}^{3/10} 3^{\frac{3(p+1)}{10}} (1+z)^{23/10} \epsilon_B^{6/5}}{t^{23/10} \eta_{300}^{11/5}}. \quad (46)$$

After shock crossing, for $\nu_a < \nu_m < \nu_c$, one has

$$\nu_a = \frac{4.4 \times 10^{12} \text{ Hz } 3^{\frac{3(p+1)}{10}} (p-1)^{8/5} A_\star^{8/7} \epsilon_B^{1/5} \eta^{48/35}}{(p-2)(1+z)^{12/35} E_{52}^{12/35} \epsilon_e \, t^{23/35}}. \quad (47)$$

For $\nu_m < \nu_a < \nu_c$, one has

$$\nu_a = 10^{19} \text{ Hz } \frac{(p-2)^{\frac{2(p-1)}{p+4}} (p-1)^{\frac{12}{p+4}}}{(p-1)^2}$$
$$\times (85.4 - 81p + 19.8p^2)(1+z)^{\frac{2(3p-2)}{7(p+4)}}$$
$$A_\star^{-\frac{5(p-10)}{14(p+4)}} E_{52}^{\frac{2(3p-2)}{7(p+4)}} \epsilon_B^{\frac{p+2}{2(p+4)}} \epsilon_e^{\frac{2(p-1)}{p+4}} \eta^{-\frac{8(3p-2)}{7(p+4)}} \, t^{\frac{-13p-24}{7(p+4)}}. \quad (48)$$

Figure 8. Same as figure 7, but for $z = 5$.

A.4. Thick Shell Wind

Before shock crossing, for $\nu_a < \nu_m < \nu_c$, one has

$$\nu_a = 3.4 \times 10^{14} \text{ Hz } 3^{\frac{3(p+1)}{10}} \frac{(p-1)^{8/5}}{(p-2)}$$
$$\times t^{-1} E_{52}^{2/5} A_\star^{2/5} \eta_{300}^{-8/5} \epsilon_e \epsilon_B^{1/5} T_{90}^{2/5}. \qquad (49)$$

For $\nu_m < \nu_a < \nu_c$, one has

$$\nu_a = 10^{17} \text{ Hz } t^{-1} E_{52}^{\frac{2-p}{2p+8}} A_\star^{\frac{2+p}{p+4}} \eta^{\frac{2p-4}{p+4}} \epsilon_e^{\frac{2p-2}{p+4}} \epsilon_B^{\frac{2+p}{2p+8}} T_{90}^{\frac{p-2}{2p+8}}. \qquad (50)$$

For $\nu_a < \nu_c < \nu_m$, one has

$$\nu_a = 4.0 \times 10^{22} \text{ Hz } 3^{\frac{3(p+1)}{10}} t^{-2} E_{52}^{-1/10}$$
$$\times A_\star^{19/10} \eta_{300}^{-3/5} \epsilon_B^{6/5} T_{90}^{1/10}. \qquad (51)$$

After shock crossing, for $\nu_a < \nu_m < \nu_c$, one has

$$\nu_a = 4.0 \times 10^{14} \text{ Hz } 3^{\frac{3(p+1)}{10}} \frac{(p-1)^{8/5}}{(p-2)} t^{-3/5} E_{52}^{2/5}$$
$$\times A_\star^{2/5} \eta_{300}^{-8/5} \epsilon_e \epsilon_B^{1/5} T_{90}^{-4/5}. \qquad (52)$$

For $\nu_m < \nu_a < \nu_c$, one has

$$\nu_a = 10^{17} \text{ Hz } t^{-\frac{26p+15}{8p+32}} E_{52}^{\frac{2-p}{2p+8}} A_\star^{\frac{2+p}{p+4}} \eta^{\frac{2p-4}{p+4}}$$
$$\times \epsilon_e^{2p-2p+4} \epsilon_B^{\frac{2+p}{2p+8}} T_{90}^{\frac{11p-14}{8p+32}}. \qquad (53)$$

APPENDIX B
ANALYTICAL EXPRESSIONS OF χ

In this appendix, we present χ values for a typical value $p = 2.2$ in two regimes: χ_h for the high-frequency (GHz) regime, and χ_l for the low-frequency (MHz) regime:

Thin shell ISM:

$$\chi_h = \frac{0.17 \,(1+z)^{1.4} \mathcal{R}_B^{0.01} \mathcal{R}_e^{0.3} \epsilon_e^{0.1}}{E_{52}^{0.25} n_0^{0.83} \epsilon_B^{0.32} \eta^{0.63}} \left(\frac{\nu_{\text{obs}}}{10^9}\right)^{1.4}; \qquad (54)$$

$$\chi_l = \frac{7.2 \times 10^{-6} \sqrt{1+z} \, \mathcal{R}_B^{0.01} \mathcal{R}_e^{0.3} \epsilon_e^{0.06} \sqrt{\nu_{\text{obs}}}}{E_{52}^{0.07} n_0^{0.3} \epsilon_B^{0.14} \eta^{0.63}}. \qquad (55)$$

Thick shell ISM:

$$\chi_h = \frac{10^{-3} \, T_{90}^{0.31} (1+z)^{1.17} \mathcal{R}_e^{0.26} \epsilon_e^{0.93} \eta^{0.04}}{E_{52}^{0.36} n_0^{0.77} \mathcal{R}_B^{0.02} \epsilon_B^{0.35}} \left(\frac{\nu_{\text{obs}}}{10^9}\right)^{1.48}; \qquad (56)$$
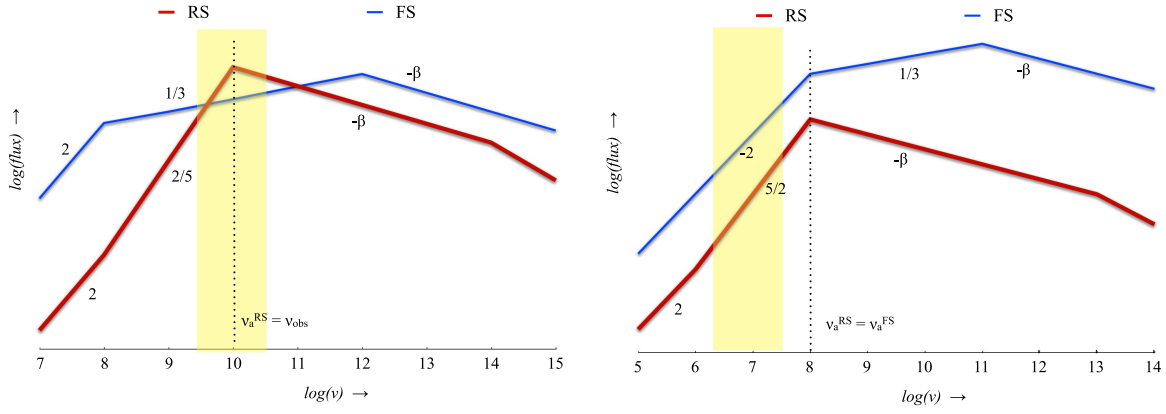
Figure 9. Sketch of FS (gray) and RS (red) spectra for typical physical parameters at (left) t_a, the peak of the GHz frequency RS light curve, and (right) $t_{\rm eq}$, the peak of the MHz frequency RS light curve. The yellow-highlighted region is the range of observing frequencies. We can see that $t_{\rm eq}$ is much later than t_a. Hence, between the two epochs, the FS f_m either remains constant (ISM) or falls off as t^{-1} (wind). The RS f_m falls far more steeply and thereby reduces the RS flux at $t_{\rm eq}$ compared to t_a. We have not considered the flux suppression due to a jet break.
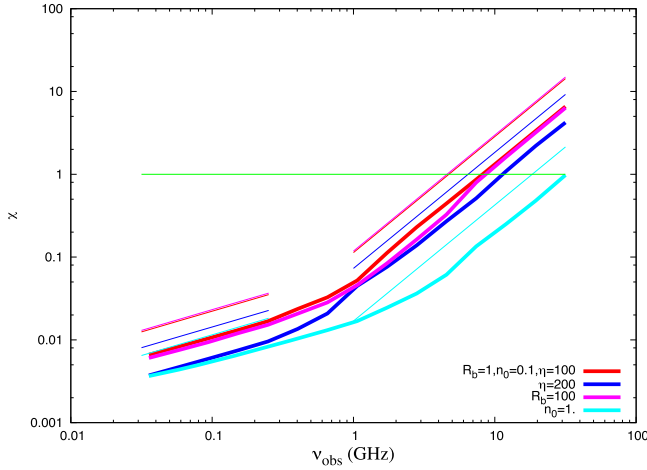

Figure 10. χ vs. $\nu_{\rm obs}$ for different sets of parameters for the thin ISM case. The thick lines show numerical results and the thin lines are analytical approximations using the formulae in Section 5.2. The difference between the two is due to the analytical approximations in evaluating the thermal energy density and number density in shocked ejecta (RS), smoothing of the synchrotron spectrum in numerical calculations, and the possibility of a jet break at $t_{\rm peak}$ in low frequencies. Red ($\mathcal{R}_B = 1$, $\eta = 100$, $n_0 = 0.1$), blue ($\mathcal{R}_B = 1$, $\eta = 200$, $n_0 = 0.1$), magenta ($\mathcal{R}_B = 100$, $\eta = 100$, $n_0 = 0.1$), and cyan ($\mathcal{R}_B = 1$, $\eta = 200$, $n_0 = 1.0$). Other parameters remain the same ($E_{52} = 5$, $\mathcal{R}_e = 1$, $\epsilon_e = 0.1$, $\epsilon_B = 1.e-3$, $\theta_j = 5°$, and $z = 1$). The horizontal line marks the detectability of RS ($\chi = 1$).

$$\chi_l = \frac{10^{-3} T_{90}^{0.31} (1+z)^{0.19} \mathcal{R}_e^{0.26} \eta^{0.04}}{E_{52}^{0.17} n_0^{0.18} \mathcal{R}_B^{0.02} \epsilon_B^{0.16} \epsilon_e^{0.05}} \sqrt{\frac{\nu_{\rm obs}}{10^9}}. \qquad (57)$$

Thin shell wind:

$$\chi_h = \frac{1.22 E_{52}^{0.9} (1+z)^{0.9} \mathcal{R}_B^{0.18} \mathcal{R}_e^{0.49} \epsilon_e^{1.16}}{A_\star^{1.62} \epsilon_B^{0.15} \eta^{1.89}} \left(\frac{\nu_{\rm obs}}{10^9}\right)^{0.9}; \quad (58)$$

$$\chi_l = \frac{0.12 \sqrt{E_{52}} \sqrt{1+z}\, \mathcal{R}_e^{0.26}}{A_\star^{0.84} \mathcal{R}_B^{0.02} \epsilon_B^{0.16} \epsilon_e^{0.06} \eta^{1.92}} \sqrt{\frac{\nu_{\rm obs}}{10^9}}. \qquad (59)$$

Thick shell wind:

$$\chi_h$$
$$= \frac{10^{-4} E_{52}^{0.4} T_{90}^{0.56} (1+z)^{0.4} \mathcal{R}_B^{0.16} \mathcal{R}_e^{0.5} \epsilon_e^{1.13} \eta^{0.08}}{\text{Astar}^{1.18} \epsilon_B^{0.17}} \left(\frac{\nu_{\rm obs}}{10^9}\right)^{0.96};$$
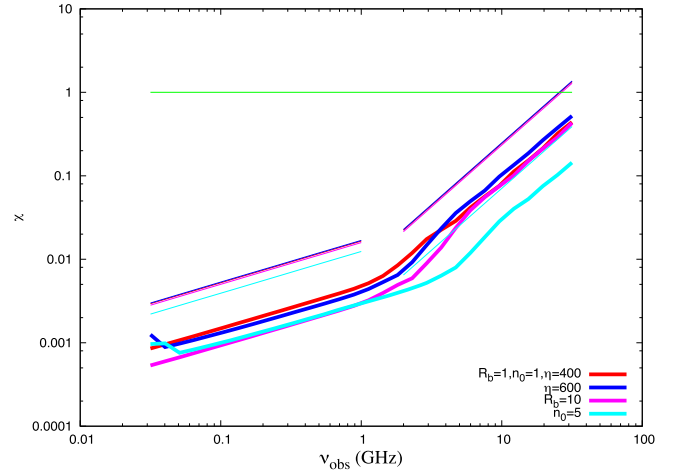$$(60)$$

Figure 11. The same as Figure 10, but for the thick ISM case. Red ($\mathcal{R}_B = 1$, $\eta = 400$, $n_0 = 1$), blue ($\mathcal{R}_B = 1$, $\eta = 600$, $n_0 = 1$), magenta ($\mathcal{R}_B = 10$, $\eta = 400$, $n_0 = 1$), and cyan ($\mathcal{R}_B = 1$, $\eta = 400$, $n_0 = 5$). Other parameters remain the same ($E_{52} = 1$, $\mathcal{R}_e = 1$, $\epsilon_e = 0.1$, $\epsilon_B = 1.e-3$, $T_{90} = 80$, and $z = 1$).
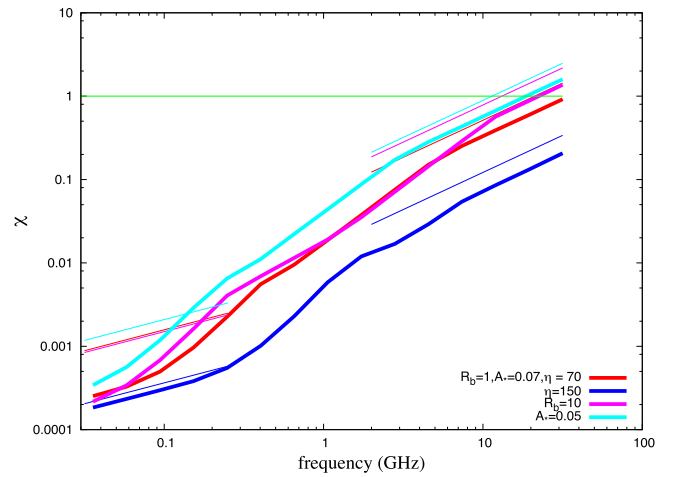

Figure 12. The same as Figure 10, but for the thin wind case. Red ($\mathcal{R}_B = 1$, $\eta = 70$, $A_\star = 0.07$), blue ($\mathcal{R}_B = 1$, $\eta = 150$, $A_\star = 1$), magenta ($\mathcal{R}_B = 10$, $\eta = 70$, $A_\star = 0.07$), and cyan ($\mathcal{R}_B = 1$, $\eta = 70$, $A_\star = 0.05$). Other parameters remain the same ($E_{52} = 5$, $\mathcal{R}_e = 1$, $\epsilon_e = 0.1$, $\epsilon_B = 8.e-5$, and $z = 1$).
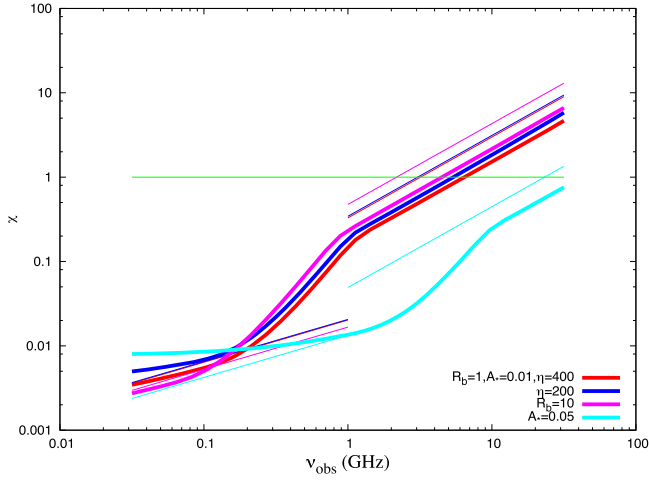
Figure 13. The same as figure 12, but for the thick wind case. Red ($\mathcal{R}_B = 1$, $\eta = 400$, $A_\star = 0.01$), blue ($\mathcal{R}_B = 1$, $\eta = 700$, $A_\star = 1$), magenta ($\mathcal{R}_B = 10$, $\eta = 400$, $A_\star = 1$), and cyan ($\mathcal{R}_B = 1$, $\eta = 400$, $A_\star = 0.05$). Other parameters remain the same ($E_{52} = 1$, $\mathcal{R}_e = 1$, $\epsilon_e = 0.1$, $\epsilon_B = 1.e-3$, $T_{90} = 80$, and $z = 1$). For the low-frequency part, the spectral regime of the numerical estimate is different to that assumed in analytical expressions.

$$\chi_l = \frac{1.2 \times 10^{-9} T_{90}^{0.56} \mathcal{R}_e^{0.19} \eta^{0.03}}{A_\star^{0.26} E_{52}^{0.06}(1+z)^{0.06}\mathcal{R}_B^{0.08}\epsilon_B^{0.18}\epsilon_e^{0.32}}\sqrt{\frac{\nu_{\mathrm{obs}}}{10^9}} . \quad (61)$$

REFERENCES

Beloborodov, A., & Uhm, Z. 2006, ApJL, 651, L1
Chandra, P., & Frail, D. A. 2012, ApJ, 746, 156
Chevalier, R., & Li, Z. 1999, ApJL, 520, L29
Fan, Y. Z., Wei, D. M., & Wang, C. F. 2004, A&A, 424, 477
Gao, H., Lei, W.-H., & Zhang, B. 2013, MNRAS, 435, 2520

Gao, H., Lei, W.-H., Zou, Y.-C., Wu, X.-F., & Zhang, B. 2013, NewAR, 57, 141
Gao, H., & Mészáros, P. 2015, AdAst, 2015, 192383
Gao, H., Wang, X.-G., Mészáros, P., & Zhang, B. 2015, ApJ, 810, 160
Ghisellini, G., Haardt, F., & Svensson, R. 1997, MmSAI, 68, 97
Gomboc, A., Kobayashi, S., Guidorzi, C., et al. 2008, ApJ, 687, 443
Harrison, R., & Kobayashi, S. 2013, ApJ, 772, 101
Japelj, J., Kopač, D., Kobayashi, S., et al. 2014, ApJ, 785, 84
Jin, Z.-P., & Fan, Y.-Z. 2007, MNRAS, 378, 1043
Kobayashi, S. 2000, ApJ, 545, 807
Kobayashi, S., Mészáros, P., & Zhang, B. 2004, ApJL, 601, L13
Kobayashi, S., & Sari, R. 2000, ApJ, 542, 819
Kobayashi, S., & Zhang, B. 2002, ApJL, 582, L75
Kobayashi, S., & Zhang, B. 2003, ApJ, 597, 455
Kopač, D., Mundell, C. G., Kobayashi, S., et al. 2015, ApJ, 806, 179
Kumar, P., & Panaitescu, A. 2003, MNRAS, 346, 905
Kumar, P., & Zhang, B. 2015, PhR, 561, 1
Laskar, T., Berger, E., Zauderer, B. A., et al. 2013, ApJ, 776, 119
Melandri, A., Kobayashi, S., Mundell, C., et al. 2010, ApJ, 723, 1331
Mészáros, P., & Rees, M. 1997, ApJ, 476, 232
Mészáros, P., & Rees, M. 1999, MNRAS, 306, L39
Mimica, P., Giannios, D., & Aloy, M. A. 2009, A&A, 494, 879
Mizuno, Y., Zhang, B., Giacomazzo, B., et al. 2009, ApJL, 690, L47
Nakar, E., & Piran, T. 2004, MNRAS, 353, 647
Nousek, J., Kouveliotou, C., Grupe, D., et al. 2006, ApJ, 642, 389
Rybicki, G. B., & Lightman, A. P. 1979, Radiative Processes in Astrophysics (New York: Wiley)
Santana, R., Barniol Duran, R., & Kumar, P. 2014, ApJ, 785, 29
Sari, R., & Piran, T. 1995, ApJL, 455, L143
Sari, R., & Piran, T. 1999a, ApJL, 517, L109
Sari, R., & Piran, T. 1999b, ApJ, 520, 641
Sari, R., Piran, T., & Narayan, R. 1998, ApJL, 497, L17
Shen, R.-F., & Zhang, B. 2009, MNRAS, 398, 1936
Troja, E., Cusumano, G., O'Brien, P. T., et al. 2007, ApJ, 665, 599
Uhm, Z. L. 2011, ApJ, 733, 86
Urata, Y., Huang, K., Takahashi, S., et al. 2014, ApJ, 789, 146
Wijers, R. A. M. J., & Galama, T. J. 1999, ApJ, 523, 177
Wu, X.-F., Dai, Z. G., Huang, Y. F., & Lu, T. 2003, MNRAS, 342, 1131
Zhang, B., Fan, Y. Z., Dyks, J., et al. 2006, ApJ, 642, 354
Zhang, B., & Kobayashi, S. 2005, ApJ, 628, 315
Zhang, B., Kobayashi, S., & Mészáros, P. 2003, ApJ, 595, 950
Zou, Y.-C., Wu, X., & Dai, Z. 2005, MNRAS, 363, 93